Measuring PETase enzyme kinetics by single-molecule microscopy

Running title: Single-molecule PETase study

Yuwei Zhang[1] and William O. Hancock[1,2 *]

[1] Department of Biomedical Engineering, Pennsylvania State University, University Park, Pennsylvania, USA
[2] Department of Chemistry, Pennsylvania State University, University Park, Pennsylvania, USA

* Corresponding author:
William O. Hancock
Email: woh1@psu.edu

Abstract:

Polyethylene terephthalate (PET) is one of the most widely produced man-made polymers and is a significant contributor to microplastics pollution. The environmental and human health impacts of microplastics pollution have motivated a concerted effort to develop microbe- and enzyme-based strategies to degrade PET and similar plastics. A PETase derived from the bacteria *Ideonella sakaiensis* was previously shown to enzymatically degrade PET, triggering multidisciplinary efforts to improve the robustness and activity of this and other PETases. However, because these enzymes only erode the surface of the insoluble PET substrate, it is difficult to measure standard kinetic parameters, such as k_{on}, k_{off} and k_{cat}, complicating interpretation of the activity of mutants using traditional enzyme kinetics frameworks. To address this challenge, we developed a single-molecule microscopy assay that quantifies the landing rate and binding duration of quantum dot-labeled PETase enzymes interacting with a surface-immobilized PET film. Wild-type PETase binding durations were well fit by a biexponential with a fast population having a 2.7 s time constant, interpreted as active binding events, and a slow population interpreted as non-specific binding interactions that last tens of seconds. A previously described hyperactive mutant, S238F/W159H had both a faster on-rate and a slower off-rate than wild-type PETase, potentially explaining its enhanced activity. Because this single-molecule approach provides a more detailed mechanistic picture of PETase enzymatic activity than standard bulk assays, it should aid future efforts to engineer more robust and active PETases to combat global microplastics pollution.

Statement of significance:

Plastic pollution is a global environmental and human health problem. PETases are recently discovered enzymes that degrade the ubiquitous plastic polyethylene terephthalate (PET). A push is underway to understand and optimize these enzymes to enable large-scale microplastics

remediation. Here, we use single-molecule fluorescence microscopy to visualize the interactions of PETase enzyme molecules with a thin film of PET. We identify specific binding interactions of a few seconds that differ between wild-type and PETase mutants that have been previously shown to have altered activities. These single-molecule investigations provide a new window into the mechanism and activity of PETase enzymes, and provide a platform for characterizing and optimizing novel PETases with improved function and stability.

Introduction

Polyethylene terephthalate (PET) is one of the most widely produced man-made polymers, and is derived from petroleum by the esterification of terephthalic acid and ethylene glycol. Accumulation of PET and other microplastics in the environment is a pressing global problem that has motivated efforts to develop microbe- and enzyme-based strategies to degrade PET (1, 2). In 2016, Yoshida *et al.* reported a newly discovered bacterium, *Ideonella sakaiensis* 201-F6, that was able to use PET as its major carbon and energy source for growth. The PETase enzyme derived from this microbe, *Is*PETase, was shown to convert PET to mono(2-hydroxyethyl) terephthalic acid (MHET), with trace amounts of terephthalic acid (TPA) and bis(2-hydroxyethyl)-TPA (BHET) as secondary products (3). This discovery set off a global interdisciplinary effort to identify, characterize and optimize PET degrading enzymes, with the hope that these biodegradation approaches can be scaled up to reduce microplastics pollution in the environment (4, 5).

Current methods to evaluate the specific activity of PETases have included analysis of PET surface erosion by scanning electron microscope (SEM), quantifying decreases in PET crystallinity using differential scanning calorimetry, and measuring product released by HPLC (6–8). These bulk assays provide quantitative information on enzyme activity, but relating these measurements to the specific enzyme kinetic parameters of the PETase enzymes is complicated by the insolubility of PET and the fact that enzymes only act on exposed surfaces. Alternatively, there are turbidimetric or colorimetric methods for PETase enzyme activity, such as the soluble substrates p-nitrophenyl acetate (pNPA) and p-nitrophenyl butyrate (pNPB), but these soluble substrates are poor analogs for crystalline PET (7, 9).

Like PETases, cellulases and cutinases are enzymes that react only with the surface of their insoluble subtrates (10). Because the effective surface: volume relationship is generally not

known, it is difficult to directly apply the Michaelis-Menten formalism to these reactions. Specifically, the resulting K_M values are not in typical molar concentrations, making it difficult to extract the bimolecular on- and off-rates, k_{on} and k_{off}, as well as the enzyme turnover rate, k_{cat}. One approach that has been used extensively on enzymes like cellulases or cutinases is to vary the enzyme concentration rather than the substrate concentration in the solution, such that enzymes partition to bound and soluble fractions (11–13). However, even here the available area, A_0, is a key parameter that must be estimated rather than precisely measured. In contrast, single-molecule approaches directly measure binding rates and durations, and thus they offer more direct access to true biochemical parameters of enzymes. Further, because the activity of the enzyme (rather than the substrate) is monitored, they sidestep the requirement of relating exposed surface area to substrate mass or volume, which bulk assays typically require. To this end, by imaging the cellulase Cel7A binding to and moving along its insoluble substrate, cellulose, we were able to extract enzyme kinetic parameters from the single-molecule tracking dynamics (14).

Previous work that used bulk enzymatic assays and molecular dynamics simulations to investigate key residues in the substrate binding cleft of *Ideonella sakaiensis* PETase identified two mutants with altered activities (6). A hyperactive mutant, S238F/W159H, was created that narrowed the substrate binding cleft towards that of native cutinase, and an impaired mutant, W185A was created by mutating a highly mobile tryptophan thought to play a role in substrate binding. The altered enzyme activities were measured by imaging the surface erosion of PET using electron microscopy and by monitoring changes in the crystallinity of the PET substrate. These experimental approaches clearly showed changes in enzyme activity, particularly the enhanced activity of the hyperactive mutant, but because the methodology did not quantify k_{on}, k_{off} and k_{cat}, it is difficult to define in enzymatic terms which transition rates are altered by the mutations.

In the present work, we measured the single-molecule binding dynamics of *Ideonella sakaiensis* PETase wild-type and both the hyperactive and impaired mutants characterized previously. We used total internal reflection fluorescence microscope (TIRFM) of quantum dot (Qdot) labeled PETase reversibly binding to glass coverslips functionalized with a thin film of PET. By measuring the residence time of the enzymes on the substrate, we calculate an apparent off-rate that provides information about both the turnover rate of the enzyme and its binding affinity to the

98 PET substrate. This work provides new insights into PETase function and introduces a new
99 approach for investigating the enzymology of other enzymes that react with insoluble substrates.

100

101 ## Materials and methods

102 ***Expression and purification of PETase enzymes***

103 DNA plasmids for wild-type PETase (PETase, *I. sakaiensis*, accession number: A0A0K8P6T7,
104 Addgene number: #112202), hyperactive mutant (Addgene number: #112203) and the impaired
105 mutant (Addgene number: #112204) were purchased from Addgene (6). Plasmids were
106 transformed into *E. coli* C41(DE3) (Lucigen) and inoculated on a Nutrient Agar plate containing
107 100 µg/mL ampicillin (VWR; Cas: 69-52-3). After culturing overnight at 37°C, single colonies for
108 each variant were inoculated into a started culture of 5 mL Terrific Broth media (Thermo Scientific)
109 containing 100 µg/mL ampicillin and grown at 37°C overnight in a 180 rpm shaking incubator.
110 Each starter culture was then transferred into 2 L flasks with 400 mL media containing 100 µg/mL
111 ampicillin and grown at 37°C at 200 rpm until the optical density at 600 nm reached 0.6-0.8.
112 Protein expression was induced by adding 1 mM isopropyl β-D-1-thiogalactopyranoside (IPTG)
113 (EMD Millipore Corp.; Cas: 367-93-1). Cells were then incubated for 18 to 20 hours at 20°C at 200
114 rpm, harvested by centrifugation at 5000 rpm for 20 min, and stored at -80°C for later purification.
115 Frozen cell pellets were resuspended in a lysis buffer (300 mM NaCl, 10 mM imidazole, 20 mM
116 Tris HCl, pH 7.4,) and lysed by sonication. Lysate was clarified by centrifugation at 45,000 rpm for
117 35 minutes. The supernatant was then applied to a 2 mL Ni Sepharose 6 Fast Flow (Cytiva) column
118 and eluted by elution buffer containing 300 mM NaCl, 300 mM imidazole, 20 mM Tris HCl, pH 7.5.

119

120 ***Microscopy and image analysis***

121 PET film (Goodfellow, UK) was cleaned in purified water by sonication, wiped with 100% ethanol,
122 cut into pieces, and dissolved in trifluoroacetic acid (TFA) (Sigma Aldrich; Cas: 76-05-1) to a
123 concentration of 1 wt%. 5-7 µL of PET solution was dripped onto a plasma cleaned coverslip,
124 covered with a second cleaned coverslip, and the two coverslips were then separated and dried

in air at room temperature for 30 min. Next, the coverslips were transferred to a 120°C oven for 20 min to achieve a smooth PET coating, followed by cooling at room temperature. Flow cells were assembled with the PET-coated coverslips using double-sided tape. The PET surface was blocked to minimize nonspecific protein adsorption by flowing 0.33 mg/mL casein into the flow cell for 3 min, followed by an enzyme solution consisting of 8 nM wild-type PETase or its mutant labeled with 0.8 nM $Qdot_{655}$ (Thermo Scientific), 2 mM 2-Mercaptoethanol (Sigma-Aldrich; Cas: 60-24-2), and 4 mM 4-Nitrophenyl acetate (Sigma-Aldrich; Cas: 830-03-5) in a buffer containing 100 mM NaCl and 50 mM sodium phosphate, pH 7.4. The $Qdot_{655}$-labeled PETase was imaged by total internal reflection fluorescence microscopy (TIRFM) using a 488 nm laser (70 mW or 150 mW) on a custom-built microscope (15). Movies began immediately before the enzyme solution was added to the flow cells. All experiments were performed at 22°C. The 10:1 enzyme:Qdot ratio was chosen because binding events were quite rare and lower ratios resulted in insufficient particle counts to accurately calculate landing rate and duration parameters.

PETase landing events and binding durations on the surface-immobilized PET film were measured by Kymograph analysis in ImageJ, as follows. Image stacks consist of a cube of x-y images at sequential times, t. First, the “Reslice” command was used to generate multiple x-t (horizontal) slices at varying y (vertical). The “Output spacing” was set to 5 pixels, which corresponds to the ~300 nm full width at half maximum of the point spread function of our microscope (15). Next, the “Grouped z projection” command was used to compress the multiple slices along the y axis into a single x-t image (see Fig. 1). From this kymograph, the binding durations are measured by the length of the vertical lines, where one pixel equals one frame, and the landing rate is measured by counting the total number of events throughout the entire movie. This approach of generating an x-t Kymograph is similar in principle to the approach of Pettersson *et al* (16). Binding duration distributions were fit to biexponentials in Python 3.9.19 using the ‘scipy.optimize’ library.

Results

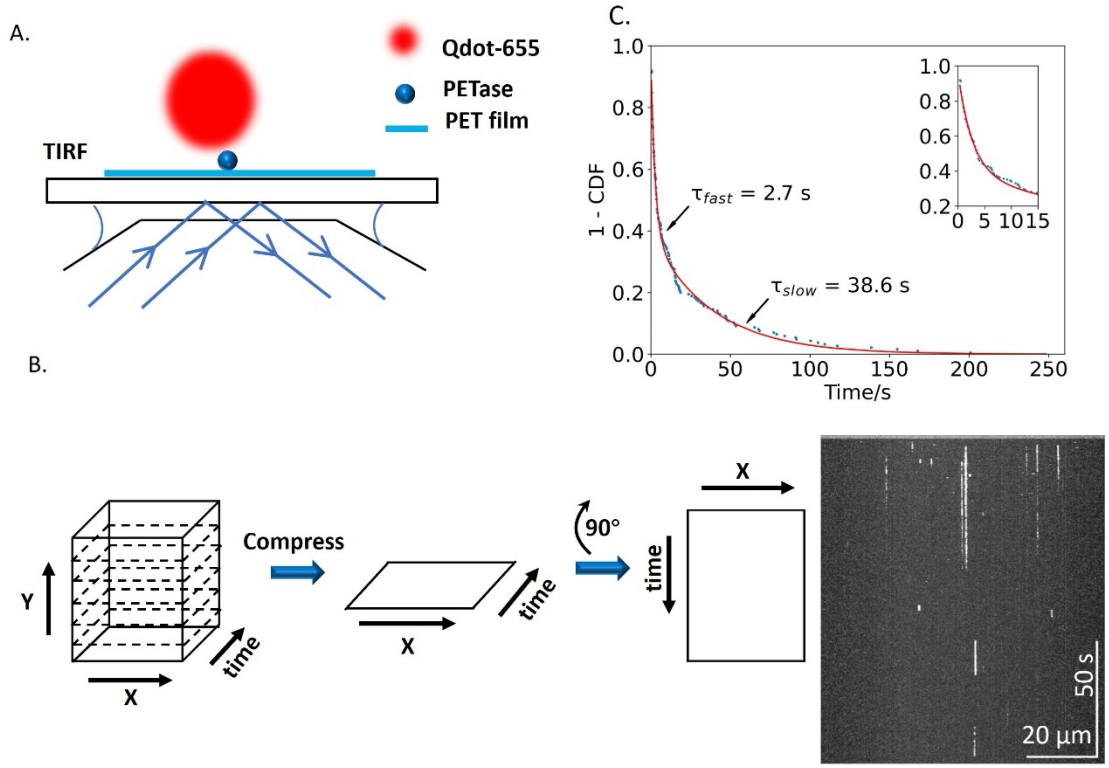

Figure 1. PETase binds reversibly to PET film. (A) Experimental design for single-molecule TIRF analysis of Qdot-labeled PETase interacting with surface-immobilized PET film. Image is not to scale. (B) Kymograph analysis. A movie, consisting of a stack of x-y images at various t is captured and resliced into x-t frames for each y, and then compressed into a single x-t image. The image is then rotated by 90° to generate a single x-t kymograph (shown at right), where vertical streaks are single-molecule binding events of varying durations. (C) Binding durations of wild-type PETase, plotted as 1 – cumulative distribution function (1-cdf). Fitting to a biexponential function reveals a fast phase, representing reversible binding interactions, as well as a slow phase. Inset: first 15 s to show details of fast phase.

Qdot$_{655}$-labeled PETase binds reversibly to PET substrate

To observe the behavior of PETase enzymes on an immobilized PET surface, PET was dissolved in trifluoroacetic acid and dripped onto the surface of a coverslip, which was then covered by another plasma cleaned coverslip to make thin PET film on the surface of both coverslips. The PET-functionalized coverslip was incorporated into a flow cell, and 0.33 mg/ml casein was flowed through to reduce nonspecific protein adsorption. *Ideonella sakaiensis* PETase (Addgene Number: #112202) (6) was bacterially expressed and biotinylated (see Methods), and combined with

169 streptavidin-coated Qdot particles at a 10:1 enzyme:Qdot ratio. The PETase-Qdot complexes were
170 then introduced into the flow cell and allowed to interact with the PET surface. Landing events
171 were imaged by total internal reflection fluorescence microscopy (TIRFM) on a custom-built
172 multimodal microscope (15), and movies were obtained of the enzymes reversibly binding to the
173 surface-immobilized PET.

174 To quantify the reversible binding interactions, we developed a kymograph-based approach (Fig.
175 1B; described in Methods) to measure the frequency and duration of PETase binding events. The
176 5 frames/s video consists of a stack of x-y images through time. The binding events in our assay
177 are focal-limited spots of diameter ~300 nm, corresponding to the point-spread function of the
178 microscope (15). Because the events are relatively rare, we can collapse a given image in y-
179 without superimposing different events. When this image is rotated by 90°, the resulting image
180 corresponds to the positions in x along the horizontal axis and time along the vertical axis (Fig.
181 1B). From this kymograph, the binding durations are measured by the length of the vertical lines,
182 where one pixel equals one frame, and the landing rate is measured by counting the total number
183 of events throughout the entire movie.

184 We found that the distribution of binding durations of wild-type PETase was well fit by a double
185 exponential function consisting of a fast phase with a time constant of 2.7 ± 0.12 s (fit ± SE of the
186 fit for all time constants) and a slow phase with a time constant of 38.6 s (Fig. 1C).

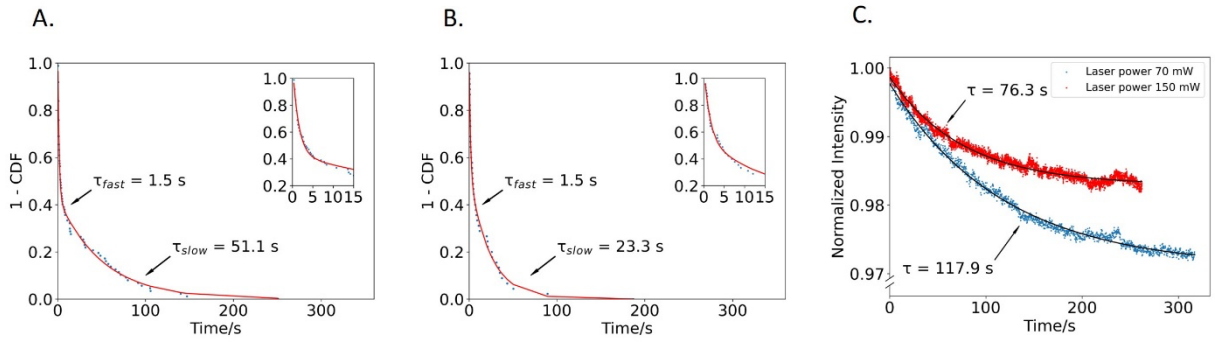

187

188 **Figure 2. Time constant of the slow phase varies with laser power.** (A) Binding durations of PETase-free Qdots at 70
189 mW illumination with biexponential fit. Inset: early times to show fast phase. (B) Binding durations of PETase-free
190 Qdots at 150 mW illumination with biexponential fit. (C) Photobleaching rates of immobilized Qdots at varying
191 illumination intensities. Particles were nonspecifically bound to the surface and the average image intensity over

192 time plotted at 70 mW and 150 mW illumination intensities. Fit to exponential fall gives time constants for Qdot
193 photobleaching of 117.9 s and 76.3 s at 70 mW and 150 mW illumination, respectively.

194

195 ***Slow binding phase is consistent with non-specific binding***

196 To better understand the origin of the fast and slow binding populations, we carried out a control
197 experiment using Qdots with no PETase bound. Using 70 mW laser power, Qdots were observed
198 to reversibly bind to the surface, and the binding durations followed a biexponential with a fast
199 phase of 1.5 ± 0.08 s (faster than the PETase fast phase of 2.7 s) and a slow phase of 51.1 ± 2.0 s
200 (Fig. 2A). We hypothesized that the slow time constant may be due to nonspecific and/or
201 irreversible binding of Qdots to the surface, with the apparent unbinding rate being due to
202 photobleaching or blinking of the Qdots. If this were the case, then increasing laser power to
203 accelerate bleaching should shorten the time constant of the slow phase. To test this, we repeated
204 the control Qdot experiment using a 150 mW laser illumination and found that the slow time
205 constant shortened from 51.1 s to 23.3 s, as expected, while the fast time constant remained at
206 1.5 s (Fig. 2B). This result is consistent with the slow phase being due to irreversible binding
207 events whose durations are truncated by photobleaching or blinking, rather than dissociation.

208 To further validate our photobleaching hypothesis, we immobilized Qdots on the surface and
209 quantified their population-level photobleaching rate. To do this, we flowed 50 pM Qdots (lacking
210 PETase) into the flow cell without first blocking the PET surface to prevent nonspecific adsorption,
211 washed away any free Qdots that did not bind, and imaged these nonspecifically-bound Qdots
212 under continuous laser illumination. The average fluorescence intensity of the image fell
213 exponentially over time due to photobleaching of the immobilized Qdots (Fig. 2C). At 70 mW laser
214 power, the time constant was 118 s, and at 150 mW laser power, the time constant fell to 76.3 s,
215 consistent with faster Qdot photobleaching at higher laser powers. This population-level result
216 reinforced our single-molecule result in Fig. 2AB, supporting our conclusion that the slow time
217 constant in the PETase experiments (Fig. 1) is due to slow photobleaching of Qdots that are
218 nonspecifically bound to the surface.

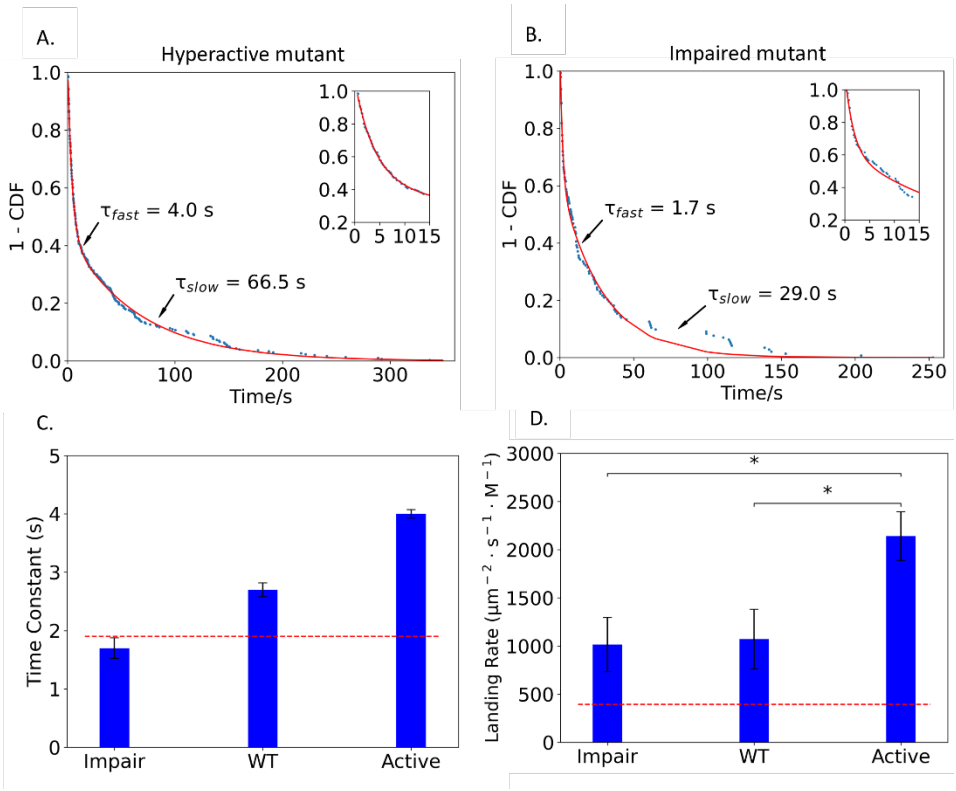

Figure 3. Hyperactive and impaired mutants have different fast-phase time constants and overall landing rates. (A) Distribution of binding durations of hyperactive PETase mutant, fit by a biexponential. Inset: first 15 s to show details of fast phase. (B) Distribution of binding durations of impaired PETase mutant, fit by biexponential. Inset: first 15 s to show details of fast phase. (C) Time constants of fast phase for wild-type (from Fig. 1C), and impaired and hyperactive mutant PETase (From Fig. 3A and B, respectively). Dashed line is time constant fast phase from Qdot control (see Fig. S1 for Qdot binding duration distribution). Error bars are standard error of the fit. (D) Single-molecule PETase landing rates, including all events independent of duration. Dashed line indicates PETase-free Qdot control landing rate. Error bars are SEM with N = 7 to 11 screens. Asterisks denote data are significantly different from one another with $p < 0.05$ by a two-sample t-test. Additionally, all landing rates were significantly different from the Qdot control (red dashed line), with $p<0.05$ by two sample t-test.

On- and off-rates of hyperactive and impaired PETases differ from wild-type

We next used our single-molecule PETase assay to investigate the reversible binding dynamics of two previously described PETase mutants. Austin *et al*. generated a hyperactive double mutant, S238F/W159H, which was designed to narrow the active site of the enzyme and was found to degrade crystalline PET more effectively than wild-type (6). They also generated an inactive mutant W185A, which was found to have impaired activity compared to wild-type PETase (6).

237 Repeating our wild-type approach, we bacterially expressed, purified, and biotinylated the two
238 mutants, adsorbed them to Qdots, and quantified their binding durations. Comparing the fast
239 phases, which correspond to reversible binding, the hyperactive mutant had a time constant of
240 4.0 ± 0.07 s (fit ± SE of the fit), longer than the wild-type (2.7 ± 0.12 s), whereas the impaired
241 variant had a time constant of 1.7 ± 0.18 s, shorter than wild-type (Fig. 3A-C). These binding
242 durations are consistent with the hyperactive mutant having a higher PET binding affinity, and the
243 impaired mutant having a lower binding affinity than wild-type.

244 To quantify the relative on-rates for PET binding, we quantified the binding frequency of the three
245 PETase enzymes along with the Qdot control (Fig. 3D). Binding rates were normalized to the
246 enzyme concentration and to the area of the microscope image. The binding rate of the impaired
247 mutant, 1014 ± 282 $\mu m^{-2} \cdot s^{-1} \cdot M^{-1}$ (mean ± SEM for N=7 movies) was similar to the wild-type rate
248 of 1070 ± 310 $\mu m^{-2} \cdot s^{-1} \cdot M^{-1}$ (N = 9). Notably, the hyperactive mutant landed more frequently, at
249 2141 ± 254 $\mu m^{-2} \cdot s^{-1} \cdot M^{-1}$ (N = 7) than wild-type. Taken together, the results suggest that the
250 hyperactive mutant achieves a higher PET binding affinity through both a faster on-rate and a
251 slower off-rate. Finally, the landing rate for the Qdot control lacking PETase was 394 ± 113 /
252 $\mu m^2 \cdot s \cdot M$ (N = 11), roughly 1/3 of wild-type PETase (Fig. 3D, dashed line). This nonspecific Qdot-
253 PET interaction in the absence of enzyme means that the observed landing rates of the three
254 enzymes are somewhat overestimated; it follows that the measured enhancement of the landing
255 rate of the hyperactive mutant is a lower limit of the effect. A rough correction for this nonspecific
256 binding fraction is to consider the dashed red line in Fig 3D as the baseline.

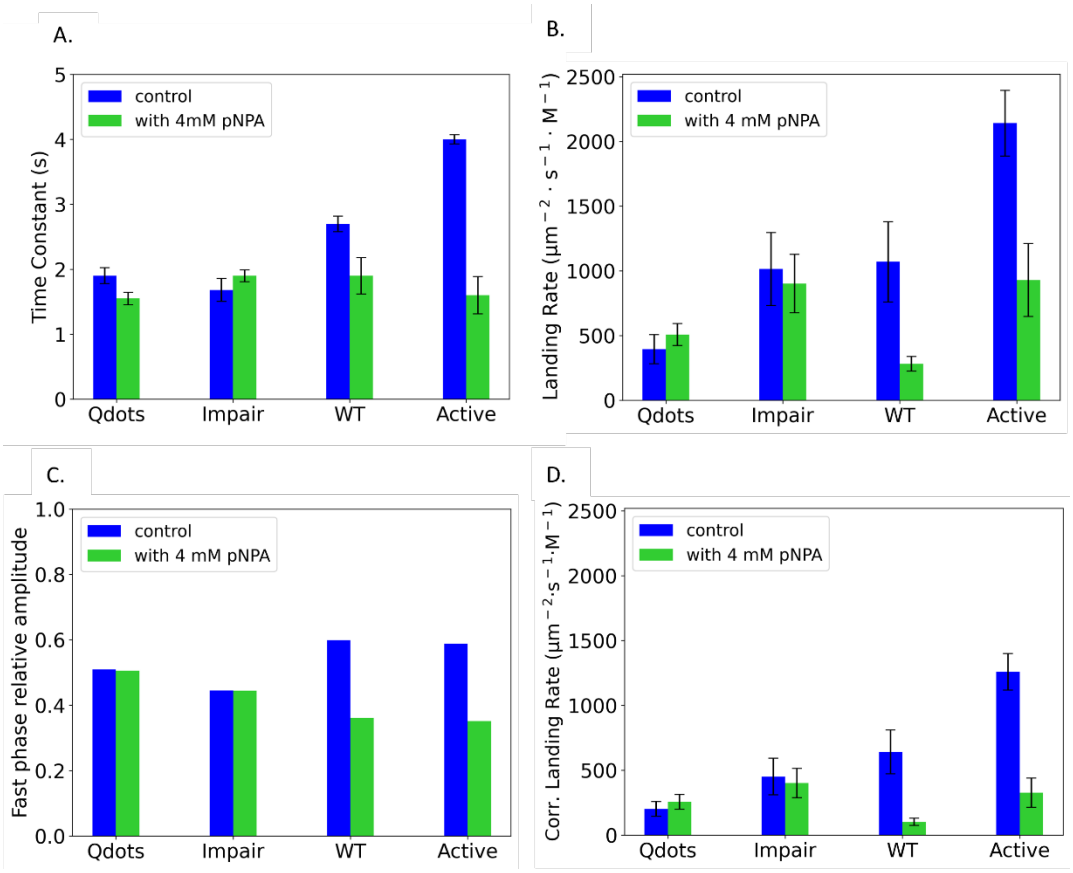

Figure 4. The competitive inhibitor pNPA blocks PETase binding to PET. (A) Time constant for fast phase of Qdot control, impaired mutant, wild-type PETase, and hyperactive mutant in the presence (green bar) or absence of 4 mM pNPA (blue bar). See Fig. S2 for binding duration distributions. (B) Overall landing rate of Qdot control, impaired mutant, wild-type PETase, and hyperactive mutant in the presence (green bar) and absence of 4 mM pNPA (blue bar). (C) Relative amplitude in biexponential fit of the fast phase for Qdot control, impaired mutant, wild-type PETase and hyperactive mutant in the absence (blue bar) and presence of 4mM pNPA (green bar). (D) Corrected landing rate (defined as the overall landing rate multiplied by the relative amplitude of the fast phase) for Qdot control, impaired mutant, wild-type PETase and hyperactive mutant in the presence (green bar) and absence of 4 mM pNPA (blue bar). Error bars are SE of the fit.

pNPA acts as a competitive inhibitor for PET binding

To more thoroughly confirm that the observed binding interactions truly reflect the enzymatic activity of the wild-type and mutant PETases, we used a PETase inhibitor to more clearly separate out specific binding from the various non-specific interactions that may be occurring. 4-Nitrophenyl acetate (pNPA) is a model soluble substrate that is used for measuring the activity of esterases including PETases (7). We reasoned that when used at high concentrations, pNPA should

273 serve as a competitive inhibitor of the PETases, occupying the active site and blocking enzyme
274 binding to the immobilized PET film. Thus, we repeated the single-molecule binding experiments
275 in the presence of 4 mM pNPA.

276 pNPA reduced the binding duration of wild-type PETase and the hyperactive variant, but had
277 negligible effect on the binding durations of the impaired mutant and the control Qdots lacking
278 bound PETase (Fig. 4A). The clear effects of pNPA on the wild-type and hyperactive PETase provide
279 further validation that the fast binding durations are reporting productive interactions of the
280 enzymes with the immobilized PET. In contrast, the finding that the binding duration of the
281 impaired mutant did not change in the presence of pNPA calls into question whether this mutant
282 is specifically binding to the immobilized PET at all under our conditions.

283 The impacts of pNPA on the landing rate mirrors the effects on the binding duration. Specifically,
284 pNPA strongly diminished the landing rate of the wild-type and hyperactive mutant, whereas it
285 had a negligible effect on the landing rate of the impaired mutant and the Qdot control (Fig. 4B).
286 To better separate out contributions to the landing rate from specific binding versus nonspecific
287 binding, we first quantified the relative amplitudes of the fast and slow phases from the
288 biexpontial fits (Fig. 4C). For wild-type and the hyperactive mutant, the amplitudes of the fast
289 durations were diminished by pNPA, consistent with the inhibitor blocking the specific (fast)
290 interactions. As expected, the relative amplitudes of the impaired mutant and the Qdot control
291 were unaffected by pNPA. In the final analysis in Fig. 4D, we multiplied the overall landing rate
292 from Fig. 4B by the relative amplitude of the fast phase from Fig. 4C. This corrected landing rate
293 corresponds to the degree to which the pNPA inhibitor blocks functional binding of the PETases
294 to the immobilized PET. In summary, the pNPA results argue that both wild-type and hyperactive
295 mutant PETase bind specifically and reversibly to the PET, with hyperactive mutant having a faster
296 relative on-rate.

297 ## Discussion

298 Despite a number of studies that have used bulk assays and computational simulations to
299 investigate the enzymatic activities of PETases, there has been little work at the single-molecule
300 level aimed at uncovering their enzymology. Because the single-molecule approaches developed
301 here enable us to measure and quantify binding events directly, they provide new information
302 that can be integrated into more comprehensive studies of the enzymology of PETases and similar
303 enzymes. These molecular insights can point to new directions for optimizing PETases to the point
304 that they can be scaled up to tackle the significant problem of microplastics pollution in the
305 environment.

306 The most challenging aspect of these single-molecule investigations was separating specific
307 binding of the enzymes from nonspecific binding by the Qdot probes. Due to autofluorescence of
308 the PET sample, labeling the PETases with standard fluorophores such as rhodamine resulted in
309 an insufficient signal-to-noise for reliable detection. Instead, we turned to Qdots, which gave a
310 very good signal-to-noise, but suffered from non-specific binding to the PET. We explored using
311 surfactants to reduce nonspecific binding but were unable to find conditions that eliminated
312 nonspecific binding while retaining specific binding. Thus, we carried out a series of control
313 experiments to determine source of the fast and slow time constants we identified in our
314 biexponential dwell times fits.

315 By characterizing Qdots lacking bound PETase and varying laser intensity to characterize
316 photobleaching, we concluded that the slow time constant (~tens of seconds) of our
317 biexponential fit to the dwell time distributions was due to nonspecific binding. The Qdot control
318 lacking any bound enzymes had a residual binding interaction with a dwell time of 1.9 ± 0.12 s,
319 but the landing frequency was substantially lower than Qdots containing a bound PETase (Fig. 3C
320 and D). This lower landing rate and the elevated binding durations of the wild-type PETase and
321 the hyperactive mutant were the first indication that the assays were detecting specific PET-
322 PETase interactions. The strongest evidence that the fast binding population was indeed specific
323 binding of the PETase to the immobilized PET was the fact that in the presence of the inhibitor
324 pNPA, both the dwell times and the landing rates of the wild-type PETase and the hyperactive

mutant fell to near the Qdot control (Fig. 4). The most important experimental result was that the mean dwell time of wild-type PETase was 2.7 s, the dwell time of the hyperactive S238F/W159H mutant was 4.0 s, and the dwell time of the impaired W185A mutant was 1.7 s, which was similar to control Qdots.

What can single-molecule imaging of enzymes tell us about their kinetic parameters? The Michaelis-Menten framework consists of a reversible binding step, with rates k_{on} and k_{off}, and a catalytic step, k_{cat}.

$$E + S \underset{k_{off}}{\overset{k_{on}}{\rightleftharpoons}} ES \xrightarrow{k_{cat}} E + P$$

The standard assumption is that product unbinding is fast relative to the catalytic step and is thus lumped into k_{cat}. For single-molecule visualization of enzymes binding to an insoluble substrate, we are visualizing the ES complex (meaning the clock starts when the fluorescent enzyme binds to the surface). What we measure is dissociation from the surface, which is described by the apparent dissociation rate, $k_{off}^{app.} = k_{off} + k_{cat}$. If we assume that the fast binding durations we measure are reflecting the residence time of the enzyme on the PET substrate, then this apparent off-rate can be calculated from our binding durations as $k_{off}^{app.} = \frac{1}{\tau_{fast}}$. From the fast time constants in Fig. 3C, $k_{off}^{app.}$ are 0.37 s^{-1} for the wild-type, 0.25 s^{-1} for the hyperactive mutant, and 0.6 s^{-1} for the impaired mutant.

The first result that comes out of this analysis is that the upper limit for k_{cat} for wild-type PETase is 0.37 s^{-1}. This conclusion comes from the fact that dissociation of the enzyme from the substrate is either through unbinding before catalysis (k_{off}) or via a catalytic event followed by dissociation from the "product" (cleaved PET in our case), with rate k_{cat}. It should be noted that the catalytic event may be considerably faster than this, meaning that the lumped k_{cat} parameter is rate-limited by product release. However, the functional turnover rate would be the same in this case, as would the apparent k_{cat} that we observed. This relatively slow turnover rate presumably is related to the crystallinity of PET film and the fact that experiments were performed at room temperature. Previous work showed that higher degrees of crystallinity lead to greater resistance of PET to enzymatic hydrolysis (17, 18). It is proposed that as temperatures approach the glass

352 transition temperature of PET, the mobility of the PET chain increases and results in more rapid
353 enzymatic hydrolysis (11, 19). Using bulk assays with the same wild-type PETase as used here,
354 Erickson et al measured a k_{cat} of 1.5 s^{-1} on amorphous PET and 0.8 s^{-1} on crystalline PET at 30 °C
355 (20), somewhat faster, but within the range of our k_{cat} of 0.37 s^{-1} at 22 °C.

356 The enzyme dissociation rates that we measure also provide insights into how mutations alter the
357 kinetic parameters of the enzymes. We interpret our data in the context of the simple Michaelis-
358 Menten model showin in Fig. 5. The hyperactive mutant, S238F/W159H was chosen by Austin *et*
359 *al.* because the mutations narrowed the active cleft of the enzyme to match that of other
360 cutinases (6). Induced fit docking simulations predicted that this double mutant would have much
361 higher affinity for PET, though no predictions were made on how the mutations may alter k_{cat}. We
362 find that $k_{off}^{app.}$ drops from 0.37 s^{-1} for the wild-type to 0.25 s^{-1} for the hyperactive mutant. First,
363 because a faster k_{cat} predicts a faster $k_{off}^{app.}$ (Fig. 5), our data argue that the greater surface erosion
364 and decrease in crystallinity seen with this mutant in a previous study (6) do not result from an
365 elevated k_{cat}. Consistent with this, Erickson et al. measured a k_{cat} of 0.5 s^{-1} for this hyperactive
366 mutant at 30 °C, slower than their wild-type k_{cat} of 0.8 – 1.5 s^{-1} in the same study (20). This value
367 at 30 °C is twice our inferred k_{cat} at 22 °C, which is reasonable agreement. However, this lower
368 k_{cat} measured by Erickson et al. seems at odds with the elevated PET surface erosion of this
369 mutant (6). One possible explanation of our slower apparent off-rate is that the rate of reversible
370 binding from the substrate, k_{off}, is slowed in the hyperactive mutant. The first effect of slowing k_{off}
371 is a lower K_M, which will improve performance at sub-saturating substrate concentrations. The
372 second effect is that for every enzyme-substrate encounter, there is a higher probability that the
373 enzyme will hydrolyze the substrate (with $p_{catalysis} = \frac{k_{cat}}{k_{cat}+k_{off}}$; Fig. 5) rather than simply
374 unbinding without acting on the substrate (with probability $p_{unbind} = \frac{k_{off}}{k_{cat}+k_{off}}$).

375 We can also use this analysis to interpret the impaired mutant. Previous work suggested that
376 residue W185 reorients upon productive binding to PET and may contribute π-stacking
377 interactions with aromatic groups in the PET substrate (6). The W185A mutation was found to
378 have reduced surface erosion activity on PET and a smaller reduction in PET crystallinity,

379 compared to wild-type (6). First, it should be noted that, because we found that τ_{fast} for the
380 impaired mutant was indistinguishable from that for Qdots alone (Fig. 3C), the $k_{off}^{app.}$ of 0.6 s^{-1} for
381 the impaired mutant should be considered a lower limit. Importantly, the landing rate of the
382 impaired mutant was considerably faster than Qdots alone (Fig. 3D), which argues that the
383 impaired mutant is not totally inactive. The simplest interpretation of the faster apparent off-rate
384 is that the off-rate of the impaired mutant from the PET substrate is considerably faster than wild-
385 type. This effect makes sense based on the proposed role of W185 in PET binding, and in bulk
386 assays would lead to a larger K_M. Another way to describe the mutation is that for every binding
387 encounter, the probability of a catalytic event, $p_{catalysis} = \frac{k_{cat}}{k_{cat}+k_{off}}$, is smaller, making the
388 enzyme less productive.

389

390 ***Conclusion and future outlook***

391 We show here that single-molecule imaging can be used to deduce kinetic parameters of PETase
392 enzymes. This approach provides a new tool that can be combined with existing bulk methods
393 and computational tools to engineer more active and robust PETases that address microplastics
394 pollution. Further development of this single-molecule approach will require reducing the non-
395 specific adsorption that complicates interpretation of the kinetic data. Potential solutions include
396 using probes other than Qdots to label the enzymes, improved processing of the PET substrate to
397 reduce the autofluorescence, and identifying surfactants or other alterations in buffer conditions
398 that minimize nonspecific binding. Notably, more active enzymes that have higher k_{cat} values are
399 predicted to bind for shorter durations, and nonspecific Qdot binding currently limits the upper
400 limit of apparent k_{off} values that can be measured. One approach that has been explored for
401 improving PETase function is attaching a Carbohydrate Binding Module (CBM) or another
402 hydrophobic domain to PETases to improve their PET binding affinities (21, 22). If such a strategy
403 is successful in creating a processive enzyme that diffuses along the surface while carrying out
404 multiple chain cleavage reactions, this activity should be measurable as both a slower apparent
405 off-rate of the enzyme measured by the current approach, as well as diffusive movements that
406 could be detected by single-molecule tracking. In conclusion, the methods developed here

407 provide a new tool for screening engineered PETases with enhanced functions, which should
408 contribute to multidisciplinary efforts to use biocatalysts to reduce microplastics pollution in the
409 environment.

410

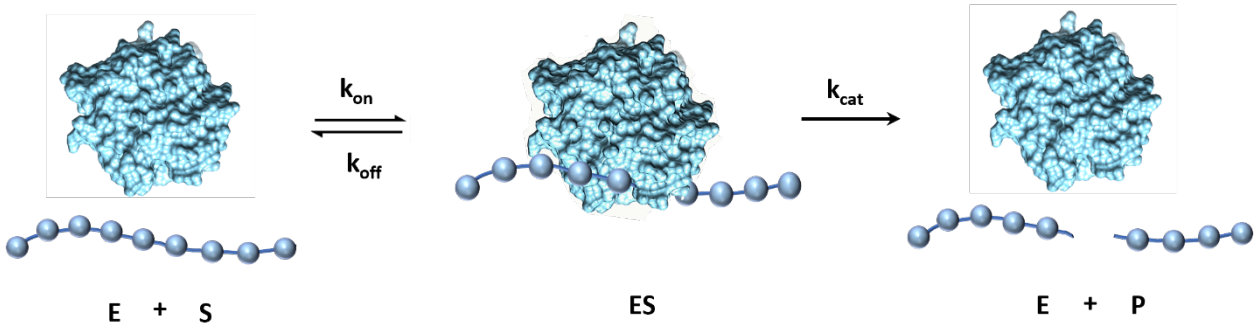

411

412 **Figure 5. Kinetic model of PETase binding to PET film.** Free PETase in solution binds to PET film reversibly with
413 association rate constant k_{on} to form an enzyme-substrate complex. The complex then either disassociates with rate
414 constant k_{off} or proceed to the PET cleavage step with turnover rate k_{cat}, followed by rapid dissociation. Qdot-labeled
415 PETase molecules bind in the ES state and dissociate with an apparent rate constant $k_{off}^{app.} = k_{off} + k_{cat}$, which is
416 equal to the inverse of the fast phase dwell time. For each binding interaction, the probability that catalysis proceeds
417 rather than the enzyme unproductively dissociating is: $p_{catalysis} = \frac{k_{cat}}{k_{cat}+k_{off}}$.

418

419 ## Acknowledgements

420 The authors thank members of the Hancock lab for helpful suggestions and Dr. Justin Brown for
421 advice in PET preparation. This work was supported by NIH grant R35GM139568.

422

423 ## References

424 1. Liu, K., T. Wu, X. Wang, Z. Song, C. Zong, N. Wei, and D. Li. 2019. Consistent Transport of
425 Terrestrial Microplastics to the Ocean through Atmosphere. *Environ. Sci. Technol.*
426 53:10612–10619.

427 2. Materić, D., H.A. Kjær, P. Vallelonga, J.-L. Tison, T. Röckmann, and R. Holzinger. 2022.
428 Nanoplastics measurements in Northern and Southern polar ice. *Environ. Res.* 208:112741.

429 3. Yoshida, S., K. Hiraga, T. Takehana, I. Taniguchi, H. Yamaji, Y. Maeda, K. Toyohara, K.
430 Miyamoto, Y. Kimura, and K. Oda. 2016. A bacterium that degrades and assimilates poly
431 (ethylene terephthalate). *Science*. 351:1196–1199.

432 4. Wei, R., G. Von Haugwitz, L. Pfaff, J. Mican, C.P.S. Badenhorst, W. Liu, G. Weber, H.P. Austin,
433 D. Bednar, J. Damborsky, and U.T. Bornscheuer. 2022. Mechanism-Based Design of Efficient
434 PET Hydrolases. *ACS Catal.* 12:3382–3396.

435 5. Oda, K., and A. Wlodawer. 2024. Development of Enzyme-Based Approaches for Recycling
436 PET on an Industrial Scale. *Biochemistry*. acs.biochem.3c00554.

437 6. Austin, H.P., M.D. Allen, B.S. Donohoe, N.A. Rorrer, F.L. Kearns, R.L. Silveira, B.C. Pollard, G.
438 Dominick, R. Duman, K. El Omari, V. Mykhaylyk, A. Wagner, W.E. Michener, A. Amore, M.S.
439 Skaf, M.F. Crowley, A.W. Thorne, C.W. Johnson, H.L. Woodcock, J.E. McGeehan, and G.T.
440 Beckham. 2018. Characterization and engineering of a plastic-degrading aromatic
441 polyesterase. *Proc. Natl. Acad. Sci.* 115:E4350–E4357.

442 7. Pirillo, V., L. Pollegioni, and G. Molla. 2021. Analytical methods for the investigation of
443 enzyme-catalyzed degradation of polyethylene terephthalate. *FEBS J.* 288:4730–4745.

444 8. Kotova, I.B., Yu.V. Taktarova, E.A. Tsavkelova, M.A. Egorova, I.A. Bubnov, D.V. Malakhova,
445 L.I. Shirinkina, T.G. Sokolova, and E.A. Bonch-Osmolovskaya. 2021. Microbial Degradation
446 of Plastics and Approaches to Make it More Efficient. *Microbiology*. 90:671–701.

447 9. Pirillo, V., M. Orlando, D. Tessaro, L. Pollegioni, and G. Molla. 2021. An Efficient Protein
448 Evolution Workflow for the Improvement of Bacterial PET Hydrolyzing Enzymes. *Int. J. Mol.*
449 *Sci.* 23:264.

450 10. Kari, J., M. Andersen, K. Borch, and P. Westh. 2017. An Inverse Michaelis–Menten
451 Approach for Interfacial Enzyme Kinetics. *ACS Catal.* 7:4904–4914.

452 11. Ronkvist, Å.M., W. Xie, W. Lu, and R.A. Gross. 2009. Cutinase-catalyzed hydrolysis of poly
453 (ethylene terephthalate). *Macromolecules*. 42:5128–5138.

454 12. Scandola, M., M.L. Focarete, and G. Frisoni. 1998. Simple kinetic model for the
455 heterogeneous enzymatic hydrolysis of natural poly (3-hydroxybutyrate). *Macromolecules*.
456 31:3846–3851.

457 13. Wei, R., T. Oeser, M. Barth, N. Weigl, A. Lübs, M. Schulz-Siegmund, M.C. Hacker, and W.
458 Zimmermann. 2014. Turbidimetric analysis of the enzymatic hydrolysis of polyethylene
459 terephthalate nanoparticles. *J. Mol. Catal. B Enzym.* 103:72–78.

460 14. Haviland, Z.K., D. Nong, K.L.V. Kuntz, T.J. Starr, D. Ma, M. Tien, C.T. Anderson, and W.O.
461 Hancock. 2021. Nanoscale dynamics of cellulose digestion by the cellobiohydrolase
462 TrCel7A. *J. Biol. Chem.* 297.

463 15. Nong, D., Z.K. Haviland, K.V. Kuntz, M. Tien, C.T. Anderson, and W.O. Hancock. 2021.
464 Integrated multi-wavelength microscope combining TIRFM and IRM modalities for imaging
465 cellulases and other processive enzymes. *Biomed. Opt. Express*. 12:3253–3264.

466 16. Pettersson, J.R., F. Lanni, and G.S. Rule. 2017. Dual Lifetimes for Complexes between
467 Glutathione- *S* -transferase (hGSTA1-1) and Product-like Ligands Detected by Single-
468 Molecule Fluorescence Imaging. *Biochemistry*. 56:4073–4083.

469 17. Chen, C., X. Han, T. Ko, W. Liu, and R. Guo. 2018. Structural studies reveal the molecular
470 mechanism of PET ase. *FEBS J.* 285:3717–3723.

471 18. Mueller, R.-J. 2006. Biological degradation of synthetic polyesters—Enzymes as potential
472 catalysts for polyester recycling. *Process Biochem.* 41:2124–2128.

473 19. Zimmermann, W., and S. Billig. 2011. Enzymes for the biofunctionalization of poly
474 (ethylene terephthalate). *Biofunctionalization Polym. Their Appl.* 97–120.

475 20. Erickson, E., T.J. Shakespeare, F. Bratti, B.L. Buss, R. Graham, M.A. Hawkins, G. König, W.E.
476 Michener, J. Miscall, K.J. Ramirez, N.A. Rorrer, M. Zahn, A.R. Pickford, J.E. McGeehan, and
477 G.T. Beckham. 2022. Comparative Performance of PETase as a Function of Reaction
478 Conditions, Substrate Properties, and Product Accumulation. *ChemSusChem*.
479 15:e202101932.

480 21. Dai, L., Y. Qu, J.-W. Huang, Y. Hu, H. Hu, S. Li, C.-C. Chen, and R.-T. Guo. 2021. Enhancing PET
481 hydrolytic enzyme activity by fusion of the cellulose–binding domain of cellobiohydrolase I
482 from Trichoderma reesei. *J. Biotechnol.* 334:47–50.

483 22. Rennison, A.P., P. Westh, and M.S. Møller. 2023. Protein-plastic interactions: The driving
484 forces behind the high affinity of a carbohydrate-binding module for polyethylene
485 terephthalate. *Sci. Total Environ.* 870:161948.

486

Supporting Information

Measuring PETase enzyme kinetics by single-molecule microscopy

Yuwei Zhang and William O. Hancock

Departments of Chemistry and Biomedical Engineering, Pennsylvania State University, University Park, Pennsylvania, USA

Figures S1-S2.

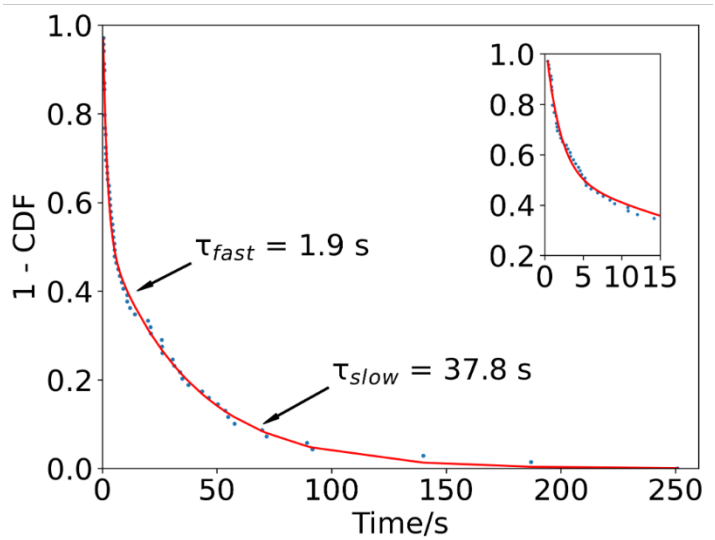

Figure S1 (related to Fig. 3): Binding durations of PETase-free Qdot control. Distribution of binding durations of Qdot control, fit by a biexponential. Inset: first 15 s to show details of fast phase.

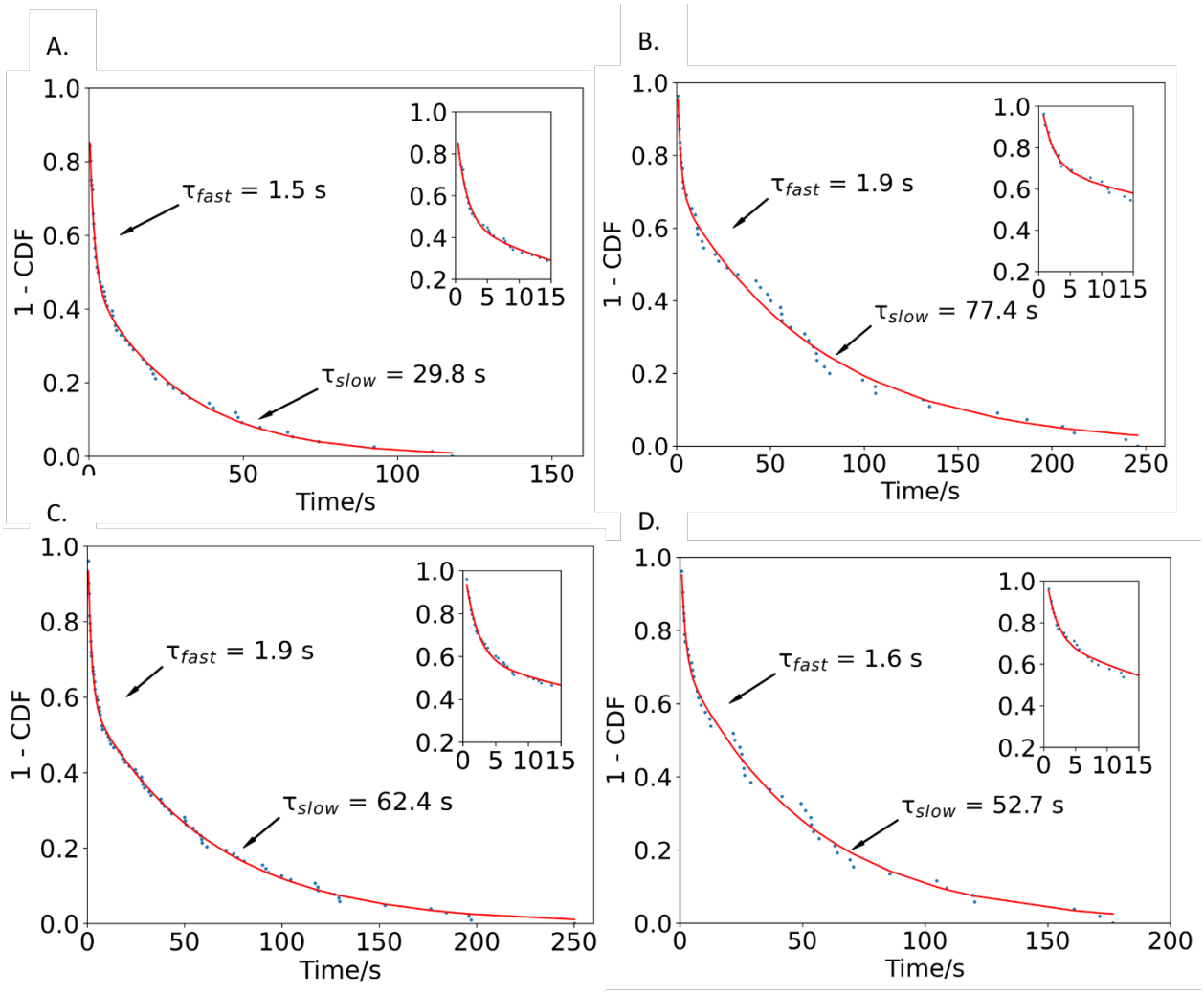

Figure S2 (related to Fig. 4): **Binding durations in the presence of 4 mM pNPA.** (A) Distribution of binding durations of Qdot control in the presence of 4 mM pNPA, fit by a biexponential. Inset: first 15 s to show details of fast phase. (B) Distribution of binding durations of wild-type PETase in the presence of 4 mM pNPA, fit by a biexponential. Inset: first 15 s to show details of fast phase. (C) Distribution of binding durations of the inactive PETase mutant in the presence of 4 mM pNPA, fit by a biexponential. Inset: first 15 s to show details of fast phase. (D) Distribution of binding durations of the hyperactive PETase mutant in the presence of 4 mM pNPA, fit by a biexponential. Inset: first 15 s to show details of fast phase.